Article

Negative Thermal Expansion Caused by the Antiferroelectric Phase Transition in Lead-Free Perovskite Ceramics

Huifen Yu [1,2], Liang Chen [1,3,*], Chang Zhou [1,4,*] and He Qi [1,3]

1   Beijing Advanced Innovation Center for Materials Genome Engineering, University of Science and Technology Beijing, Beijing 100083, China
2   School of Mathematics and Physics, University of Science and Technology Beijing, Beijing 100083, China
3   Department of Physical Chemistry, University of Science and Technology Beijing, Beijing 100083, China
4   State Key Laboratory for Advanced Metals and Materials, University of Science and Technology Beijing, Beijing 100083, China
*   Correspondence: chenliangustb@163.com (L.C.); changzhou@ustb.edu.cn (C.Z.)

Abstract: Due to the structural stability and high adjustability of perovskite, lead-free perovskite ceramics are widely thought to be one of the most promising functional materials. In this work, an abnormal negative thermal expansion behavior with a linear expansion coefficient of -54.95 ppm/K is achieved in the $(1-x)NaNbO_3$-$xCaZrO_3$ system by driving the antiferroelectric phase transition from orthorhombic phase and tetragonal phase. The NTE mechanism is verified by temperature-dependent high-energy synchrotron X-ray diffraction, dielectric spectra, and Raman scattering spectroscopy. The relationship between the antiferroelectric phase transition and negative thermal expansion behavior is systematically revealed by analyzing the evolution of the phase structure with temperature. This novel negative thermal expansion feature caused by the antiferroelectric phase transition provides new guidance for designing more negative thermal expansion materials.

Keywords: lead-free perovskite ceramics; $NaNbO_3$; antiferroelectric phase transition; negative thermal expansion

1. Introduction

Due to the stable structure, flexible composition selection, easy adjustment and preparation, and excellent properties, perovskite ceramic materials have attracted considerable attention [1]. Ferroelectric perovskite ceramics have the characteristics of switchable spontaneous polarization, leading to multifunction properties such as high permittivity, pyroelectric, strain, and piezoelectric, which make them applicable in various functional devices [2]. For a long time, Pb-based ceramics have dominated the market because of their superior properties [3–5]. However, the toxicity of the heavy metal lead is harmful to the ecological environment and the human body [6,7]. In this context, the research on lead-free perovskite ceramics, such as $BaTiO_3$ (BT), $Bi_{1/2}Na_{1/2}TiO_3$ (BNT), $K_{0.5}Na_{0.5}NbO_3$ (KNN), $BiFeO_3$ (BFO), and $NaNO_3$ (NN) [8,9], has made great progress in recent years [10].

The phase structure of ferroelectric ceramics is essential to obtaining excellent properties. Especially during thermal-induced phase transitions in perovskite ceramics, anomaly lattice distortion changes along with polarization vector changes would usually lead to a dramatic alteration in the crystal structure, cell parameters, and other physical properties such as piezoelectric, ferroelectric, dielectric, pyroelectric, and electromechanical coupling performance. For example, the $0.905Pb(Zn_{1/3}Nb_{2/3})O_3$–$0.095PbTiO_3$ ceramics, with a phase transition of rhombohedral-to-tetragonal near room temperature, exhibited a high dielectric constant and excellent piezoelectric properties [11,12]. For $0.675Pb(Mg_{1/3}Nb_{2/3})O_3$–$0.325PbTiO_3$, a significant contribution of the phase transition to dielectric and pyroelectric behavior was observed [13]. As for lead-free ceramics, they usually have a polymorphic phase transition [6]. In $(Ba_{0.91}Ca_{0.08}Sr_{0.01})(Ti_{0.92}Sn_{0.08})O_3$,

the polymorphic phase transition behavior from the orthorhombic phase to the tetragonal phase significantly enhanced electric properties [14]. For $Na_{0.47}K_{0.47}Li_{0.06}NbO_3$, due to the polymorphic phase transition from orthorhombic to tetragonal around room temperature, it exhibited good fatigue-free ferroelectric properties and high pyroelectric coefficients [15].

Ferroelectricity sometimes causes negative thermal expansion (NTE) behaviors, which are also related to ferroelectric phase transitions, and have been extensively studied in ferroelectric materials [16]. In $PbTiO_3$ ferroelectrics, NTE behavior was observed during the tetragonal-to-cubic phase transition [17]. In $Pb(Zn_{2/3}Nb_{1/3})O_3$ ceramics, a slight NTE behavior occurred in a small temperature range of the phase transition from rhombohedral to cubic [18]. The advent of NTE materials has made it possible to eliminate the thermal expansion of materials as well as regulate the coefficient of thermal expansion (CTE) of materials in practical applications [19]. Materials with NTE properties can be chemically regulated to obtain zero thermal expansion materials, or they can be added as thermal expansion inhibitors to metals, ceramics, and resins with positive thermal expansion to obtain low thermal expansion materials, thus attracting much attention from researchers [16]. However, few studies have reported the NTE phenomenon caused by the antiferroelectric phase transition in lead-free perovskite ceramics. Although some attempts have been made, such as the reported NTE behavior of $K_{0.5}Na_{0.5}NbO_3$ at 410–434 °C with a linear thermal expansion coefficient of -8.16 ppm/K, the associated NTE mechanism is still unclear [20].

The environment-friendly ferroelectric material NN has been widely studied due to its unique crystal structure and excellent electrical properties [21,22]. Pure NN undergoes a series of complex polymorphic phase transitions over a wide temperature range. It is generally believed that seven stable phases and several metastable phases exist in NN during cooling, which are named U, T2, T1, S, R, P, and N phases [23,24]. Partial works of literature have shown that the P phase consists of three different phases: the monoclinic (Pm) phase, the incommensurate phase, and the orthorhombic (Po) phase [22]. Recent studies suggest that the R phase region consists of an antiferroelectric tetragonal W phase and an antiferroelectric orthorhombic R phase [25]. At room temperature, NN exhibited an antiferroelectric P phase with orthorhombic symmetry (the space group is Pbma) [23,24]. However, due to the similar free energy of the antiferroelectric P phase and ferroelectric Q phase, a metastable ferroelectric Q phase with space group $P2_1ma$ is normally induced by an external electric field. Antiferroelectric P phase and ferroelectric Q phase coexisted in a wide temperature range [26].

In this work, the antiferroelectric stability of NN ceramics is improved by doping $CaZO_3$ (CZ) [27,28], and the $(1-x)NaNbO_3-xCaZrO_3$ system is chosen as the research object. The abnormal NTE properties of 0.91NN-0.09CZ ceramic in the temperature range of 460–470 K are reported for the first time in terms of temperature-dependent XRD, dielectric, and Raman spectra, which should be mainly ascribed to the phase transition from antiferroelectric orthorhombic P phase to antiferroelectric tetragonal W phase in 0.91NN-0.09CZ ceramic on heating near 460 K. Consequently, a contraction of the *a*-axis and an increase in tetragonality (*c/a*) appear during this antiferroelectric-antiferroelectric phase transition process, resulting in the appearance of NTE behavior.

2. Experimental Methods

Dense $(1-x)NaNbO_3-xCaZrO_3$ $((1-x)NN-xCZ, x = 0\sim0.12)$ ceramic samples were prepared by the conventional solid-state method using high-purity Na_2CO_3 ($\geq99.9\%$), $CaCO_3$ ($\geq99.5\%$), Nb_2O_5 ($\geq99.9\%$) and ZrO_2 ($\geq99.9\%$)(Sinopharm Chemical Reagent Co., Ltd., CN) as raw materials. Firstly, stoichiometric amounts of Na_2CO_3, $CaCO_3$, Nb_2O_5, and ZrO_2 powders were added to the ball mill jar, and ball milled for 8 h together with anhydrous ethanol and ZrO_2 ball media. After drying, the mixed powders were calcined at 850 °C for 5 h. Then these calcined powders were added with 0.5 wt.% of PVB binder and ball-milled again for 8 h. The powders were pressed into pellets with a diameter of 8 mm and a thickness of about 1 mm. After removing the binder PVB at 550 °C, it continues to be sintered at 1360–1400 °C for 2 h.

The prepared ceramic pellets were ground into powder to identify the crystal structure utilizing an X-ray diffractometer (XRD, PANalytical, X'Pert PRO, Almelo, The Netherlands) with Cu Kα radiation. Raman spectra at different temperatures were collected on well-polished pellets by 532 nm excitation using a Raman spectrometer (Raman, Horiba Jobin Yvon HR800, Paris, France) equipped with a heating stage (Linkam, THM 600, Tadworth, UK). Temperature-dependent XRD measurements were performed with Cu Kα radiation at an acceleration condition of 40 kV and 30 mA (D/MAX2500V; Rigaku, Tokyo, Japan). Synchrotron XRD (SXRD) measurements were performed at Argonne National Laboratory (λ = 0.458 Å). For morphological observation, the ceramics were subjected to thermal etching. The polished ceramics were placed in a muffle furnace and heated up to 1350 °C at 10 °C per minute and held for 30 min. The surface morphology of the thermally etched sample was characterized by a scanning electron microscope (SEM, LEO1530, ZEISS SUPRA 55, Oberkochen, Germany), and the distribution of chemical elements was analyzed using an energy-dispersive spectrometer (EDS). Domain morphology observations were performed on a field-emission transmission electron microscope (FE-TEM, JEM-2100, JEOL, Tokyo, Japan) at an acceleration voltage of 200 kV. For electrical characterization, the sintered ceramic samples were polished and coated with silver paste and then fired at 600 °C for 30 minutes. Temperature and frequency-dependent dielectric properties were measured using an LCR meter (Agilent E4980A, Santa Clara, CA, USA). The temperature-dependent linear thermal expansion data of samples were obtained using a NETZSCH Dilatometer (DIL 402 Expedis Select).

3. Results and Discussion

Figure 1a shows the room-temperature conventional XRD patterns of (1-x)NN-xCZ ceramics in the 2θ range of 20–60° (Figure 1b in the 2θ range of 46–47°). All the studied samples exhibit a pure perovskite structure without a second phase, implying that both Ca^{2+} and Zr^{2+} ions have successfully dissolved into the NN lattice and formed stable solid solutions for all compositions. It is well known that pure NN ceramics have an orthorhombic symmetry antiferroelectric P phase at room temperature. As seen in Figure 1b, the components with $x \leq 0.09$ show orthorhombic structure with the splitting between the two diffraction peaks of (200) and (002). As the $CaZrO_3$ content continues to increase, the split (200) peaks merge together, and all split peaks in Figure 1a become single peaks, which is similar to the pseudocubic phase structure. The relevant literature has reported that the component with $x \geq 0.1$ is not a pseudocubic phase but a local ferroelectric structure [27]. The antiferroelectricity is enhanced when a small amount of CZ is added to NN, but the continued addition of excess CZ would enhance the antiferrodistortion and induce the relaxor ferroelectric Q phase with P2$_1$ma structure when the CZ content reached 0.1 [27].

Raman spectroscopy is a more powerful tool than XRD for detecting local crystal structures, short-range ordering, and, more specifically, cationic occupancy sites [29,30]. Because it is sensitive to the change of combination bonds directly caused by molecular vibrations, it is widely used for phase transition studies of perovskite materials [31,32]. The room-temperature Raman spectra of (1-x)NN-xCZ ceramics are shown in Figure 1c. NN ceramics are orthorhombic symmetry antiferroelectric P phases at room temperature, and the space group is Pbma. According to group theory, the Pbma symmetry has a total of 60 possible Raman active modes [33]. In fact, due to the weak intensity and very small frequency difference between some modes, the number of Raman peaks observed in experimental spectra is usually less than the expected number. In order to better detect the change of all Raman bands, the observable Raman vibrations can be divided into the independent translational vibration modes of the A-site cations and the internal oxygen octahedral modes (υ_1, υ_2, υ_3, υ_4, υ_5, and υ_6) [34]. The bands with a wave number below 100 cm^{-1} are associated with the A-site vibration [35]. The split Raman peak that appears near 65 cm^{-1} at pure NN can be seen in Figure 1d, which is caused by the off-centering displacement of the part of the A-site cations [25]. When x = 0.05, the two peaks merge together, indicating the disappearance of the off-centering displacement of the A-site

cations. For wavenumbers between 100 cm^{-1} and 400 cm^{-1}, the bands are principally corresponding to the complex BO$_6$ tilt and B-site displacement [35,36]. With the increase of CZ, the contraction of these vibration peaks in the range of 100~400 cm^{-1} related to the B-O bond can be observed, indicating that the displacement of the B-site is changed. According to the deconvolution results in Figure 1e, the number of vibration peaks changes significantly at $x = 0.09~0.10$, indicating that the structure has changed. In general, due to the doping of CZ, the gradual removal of ferroelectricity is caused by the off-centering displacement of A-site cations, which promotes and stabilizes the antiferroelectric P phase at room temperature [25].
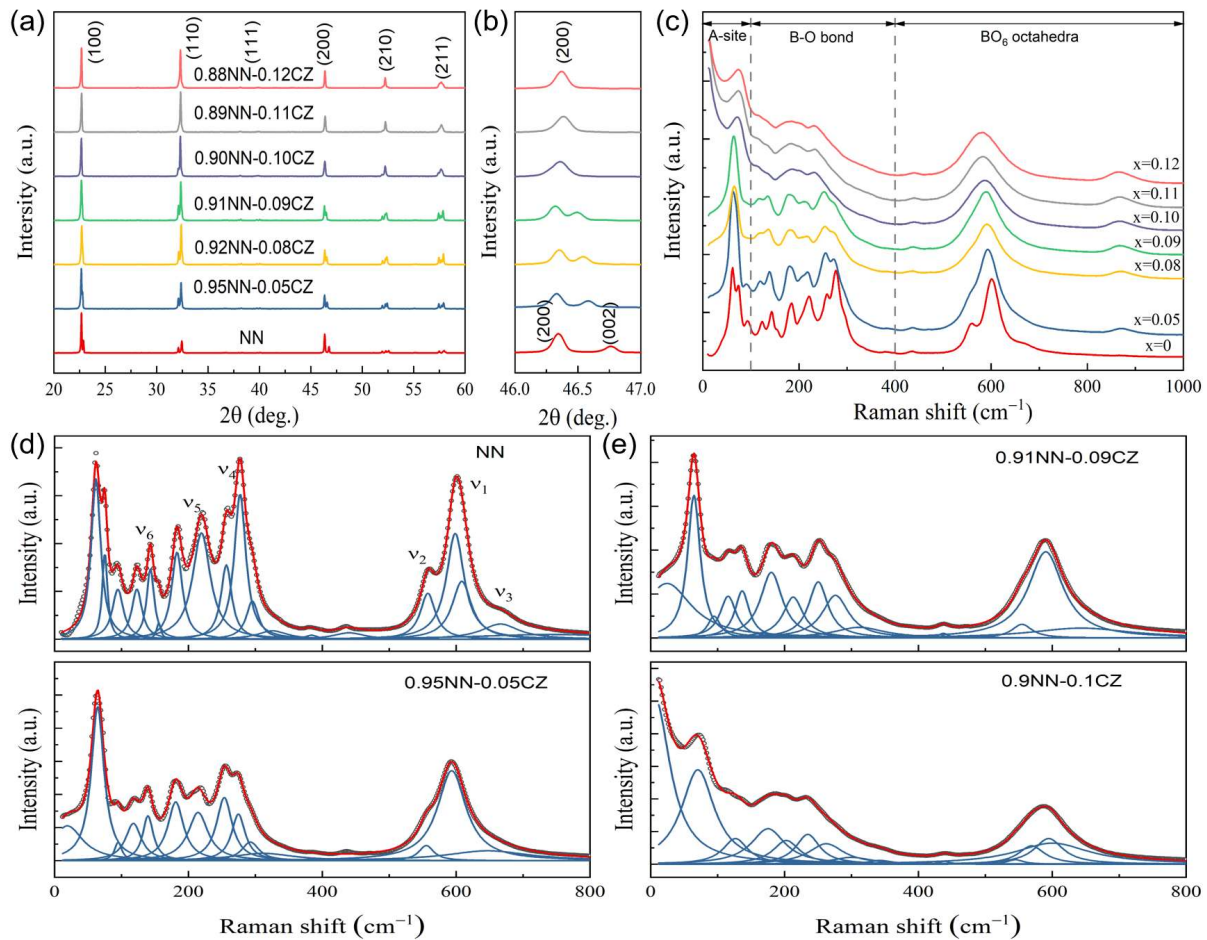

Figure 1. XRD patterns of the (1-x)NN-xCZ ceramic in the 2θ range of (**a**) 20–60° and (**b**) 46–47°. (**c**) Room-temperature Raman spectra for (1-x)NN-xCZ ceramics. Raman Gaussian-Lorentzian fitting of (**d**) the NN and 0.95NN-0.05CZ samples and (**e**) the 0.91NN-0.09CZ and 0.9NN-0.1CZ samples.

The temperature-dependent dielectric spectra of (1-x)NN-xCZ ceramics at 1 MHz are presented in Figure 2. Pure NN ceramics have a clear dielectric peak around 650 K. It is typically attributed to the phase transition of the antiferroelectric structure from the orthorhombic R phase with Pbnm space group to the orthorhombic P phase with Pbma space group [37,38]. The phase transition temperature is determined as T_{P-R}. With increasing CZ, both T_{P-R} and the maximum dielectric constant ε_m decrease. When the content of CZ reaches 0.09, T_c decreases from 650 K to 460 K. Meanwhile, the dilatometric studies on 0.91NN-0.09CZ ceramic are carried out in the temperature range of 300–550 K, and the variation of linear thermal expansion is also shown in Figure 2. There is an NTE behavior at 460–470 K, and the linear thermal expansion coefficient is −54.95 ppm/K. Since the overlap between the NTE temperature region and the phase transition temperature region can be clearly seen in Figure 2, it is preliminarily judged that the NTE behavior

is related to the dielectric anomaly of 0.91NN-0.09CZ component near 460 K. The other temperature ranges all show positive thermal expansion.
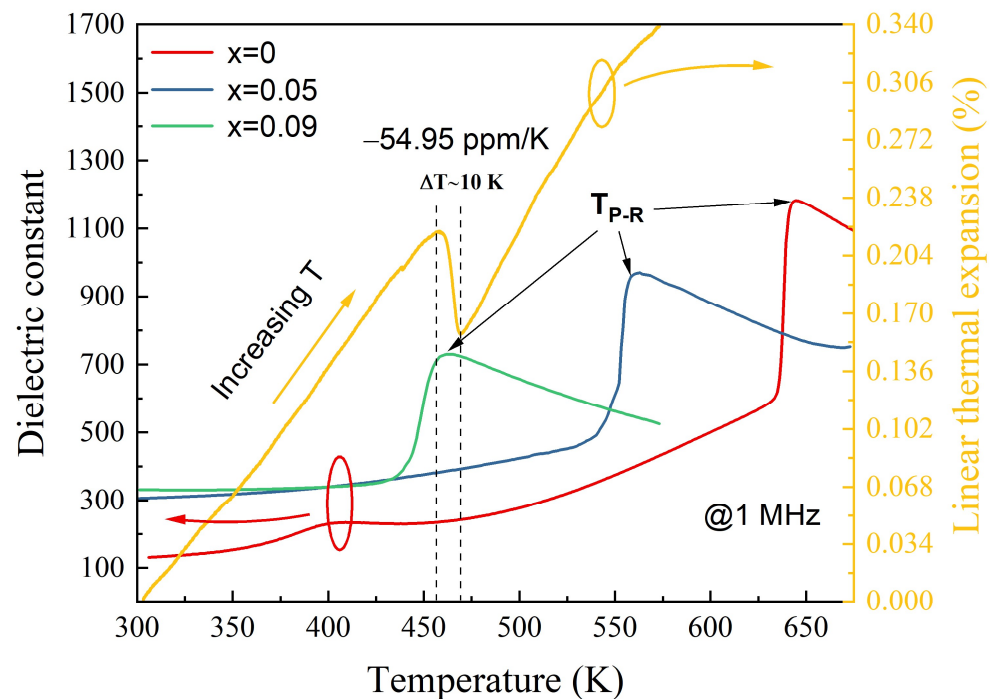

Figure 2. Temperature-dependent dielectric permittivity for (1-*x*)NN-*x*CZ ceramics at 1 MHz and linear thermal expansion for 0.91NN-0.09CZ ceramic.

The results of measuring the length of bulk samples as a function of temperature by means of dilatometry represent an apparent value of CTE, which is unavoidably affected by extrinsic factors such as microcracks, pores, and grain boundaries [16]. To explore the quality of the sintered ceramics, the morphology and the EDS images measured on the surface of the thermally etched 0.91NN-0.09CZ ceramic at the optimum sintering temperature are given. As observed in Figure 3a, dense microstructure without obvious pores can be clearly found in 0.91NN-0.09CZ ceramic, demonstrating good sample quality. According to the statistical result, 0.91NN-0.09CZ ceramic has a relatively uniform grain size distribution, with the average grain size (G_a) ~7.42 μm. The EDS images measured on the surface of the 0.91NN-0.09CZ sample are shown in Figure 3b. The results exhibit that the sample not only has a dense contact grain boundary structure but also has a homogeneous element distribution between the grains and grain boundaries, which proves that the quality of the sample is good, and the study of thermal expansion by apparent measurement is reliable.

It is recognized that thermal expansion performance mainly comes from the change of internal microstructure. In order to achieve a deep understanding of the structure, the domain morphology of the 0.91NN-0.09CZ sample is displayed in Figure 3c,d. The polydomain morphology, exhibiting a hierarchical structure feature, can be observed. These domains are typical submicron-sized stripe domains that relate to the orthorhombic phase of the sample [27]. In addition, according to the high-resolution TEM images of the lattice fringes along [1 0 0]$_C$ in Figure 3e, the 0.91NN-0.09CZ sample exhibits a good crystalline quality.
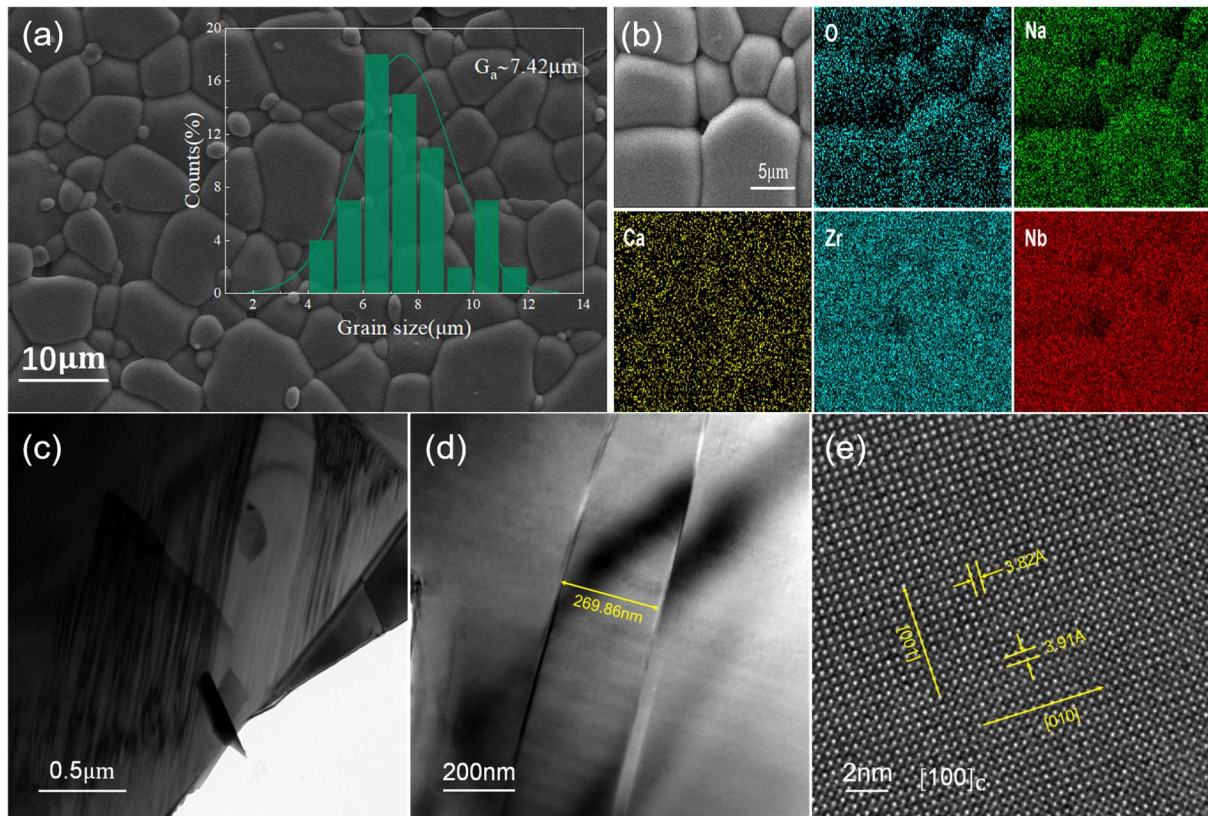
Figure 3. (**a**) SEM micrograph and grain size distribution on the polished and thermally etched surface of 0.91NN-0.09CZ ceramic. (**b**) EDS images measured on the surface of 0.91NN-0.09CZ ceramic. (**c**,**d**) Room-temperature bright-field TEM images, and (**e**) high-resolution TEM images of the lattice fringes observed along [1 0 0]$_C$ of 0.91NN-0.09CZ ceramic.

To better track the phase transition behavior of the 0.91NN-0.09CZ sample, the temperature-dependent X-ray diffraction data in the temperature range of 300–550 K is presented in Figure 4a. The XRD pattern at 300 K indexed to the orthorhombic symmetry antiferroelectric P phase, which is consistent with the previous analysis. Further increasing the temperature causes a gradual change in the diffraction peaks, especially in the 2θ range of 46.20–46.70° (Figure 4b). It is worth noting that with the increase in temperature, the two diffraction peaks (200) and (002) gradually transform into (002) and (200) peaks, which are the characteristic peaks of the tetragonal phase. Due to the insufficient resolution of the temperature-dependent XRD, the (002) and (200) splitting peaks of the tetragonal phase are not clear, and further high-energy synchrotron XRD was performed at several temperature points (Figure 4c). It can be clearly seen that a tetragonal phase exists when T = 500 K. Therefore, the dielectric anomaly of the 0.91NN-0.09CZ component near 460 K in Figure 2 belongs to the phase transition from the antiferroelectric orthorhombic P phase to the antiferroelectric tetragonal W phase. As the temperature continues to rise to 550 K, the two (002)/(200) diffraction peaks gradually shift closely and merge into a single (200) peak, implying the transition from the tetragonal phase to the pseudocubic phase. Figure 4d plots the detailed lattice parameters in the temperature range of 300–550 K by peak fitting analysis. The a_O axis and c_O axis increase almost linearly in the orthorhombic phase region, but then the a_O axis suddenly decreases around 455 K, and the c_O axis still maintains an increasing trend. For the tetragonal phase, the lattice parameters exhibit an opposite trend, with the c_T axis decreasing first and then increasing when it reaches 455 K, while the a_T axis always keeps increasing. Finally, the lengths of the a, b, and c axes are equal at 550 K. The change in unit cell volume calculated by lattice parameters is presented in Figure 4e. During the orthorhombic-to-tetragonal phase transition, NTE occurs in a

narrow temperature range, and a relatively obvious volume contraction can be observed. The results are consistent with the thermal expansion phenomenon in Figure 2, which confirms that the antiferroelectric phase transition of 0.91NN-0.09CZ ceramic is related to the appearance of NTE properties. As temperature increases, the progressively large *c/a* implies large lattice distortion, which may lead to large volume shrinkage and high lattice energy release, resulting in a large NTE. Despite the narrow temperature range, it should be noted that the NTE in 0.91NN-0.09CZ is relatively strong. This suggests that 0.91NN-0.09CZ ceramic has the potential to modulate the CTE of the material.
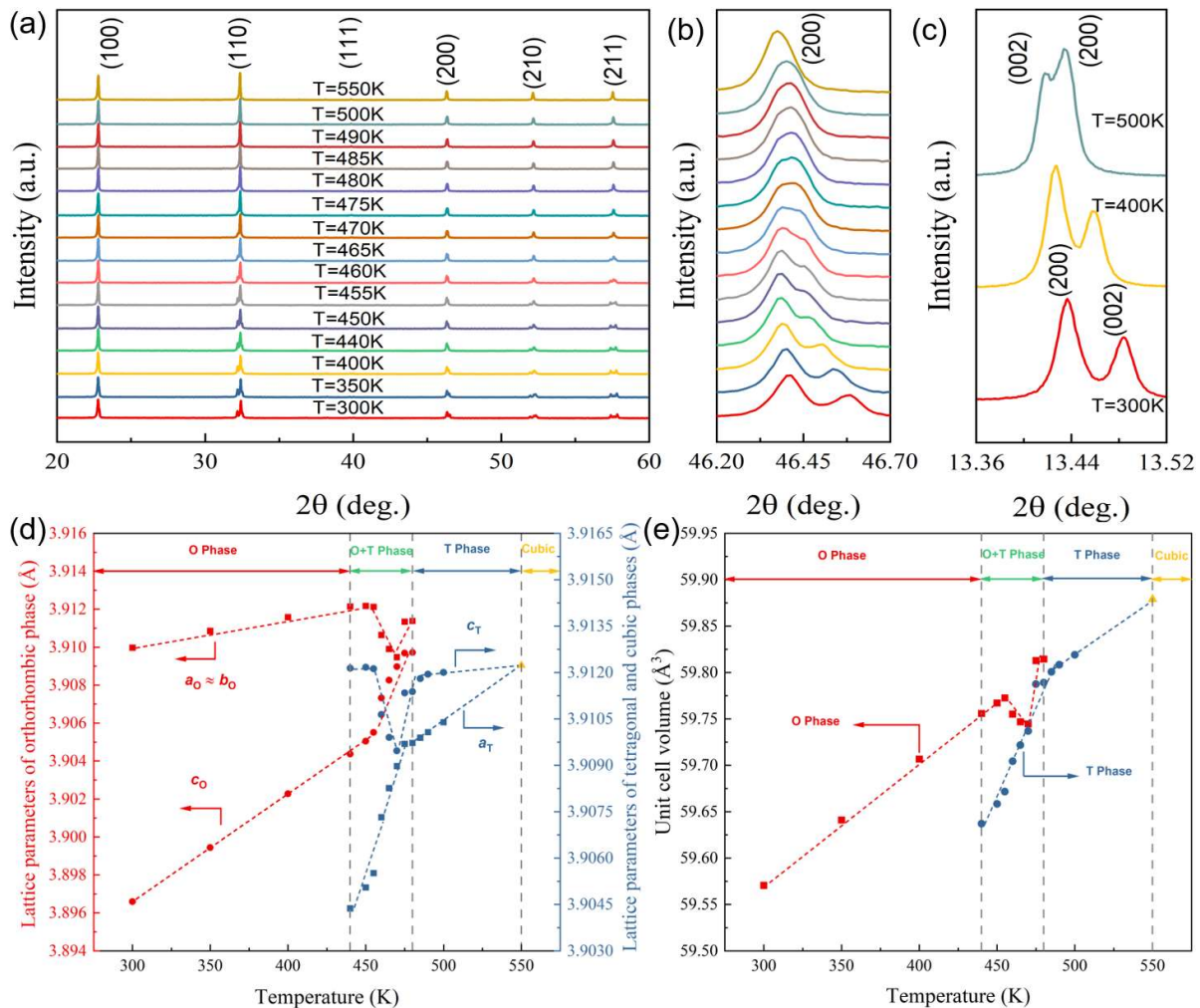

Figure 4. Temperature dependence of X-ray diffraction patterns of 0.91NN-0.09CZ ceramic in the 2θ ranges of (**a**) 20–60° and (**b**) 46.20–46.70°. (**c**) High-energy synchrotron X-ray diffraction patterns of 0.91NN-0.09CZ ceramic in the 2θ range of 13.36–13.52°. Temperature dependence of (**d**) the lattice parameters and (**e**) the unit cell volume for the 0.91NN-0.09CZ sample.

In order to further clarify the phase structure evolution behavior of 0.91NN-0.09CZ ceramic, high-temperature Raman was measured and analyzed. Figure 5a shows the temperature-dependent Raman spectra of the 0.91NN-0.09CZ sample. The Raman deconvolution results were performed using the Gaussian-Lorentzian function, and the temperature dependence of the wave number of the selected Raman peaks is displayed in Figure 5b based on the fitting results. When the temperature increases from 460 K to 465 K, the Raman peaks below 100 cm^{-1} associated with the A-site vibration change significantly, while the vibration peaks associated with the B-O bond between 100 cm^{-1} and 400 cm^{-1} contract. The apparent change in the number of vibration peaks at 460–465 K is associated with the dielectric anomaly near 460 K, as shown in Figure 2. Therefore, the phase transition

from the antiferroelectric orthorhombic P phase to the antiferroelectric tetragonal W phase near 460 K is further confirmed, which causes *a*-axis contraction, lattice distortion, and reduction of the cell volume, resulting in the abnormal NTE behavior.
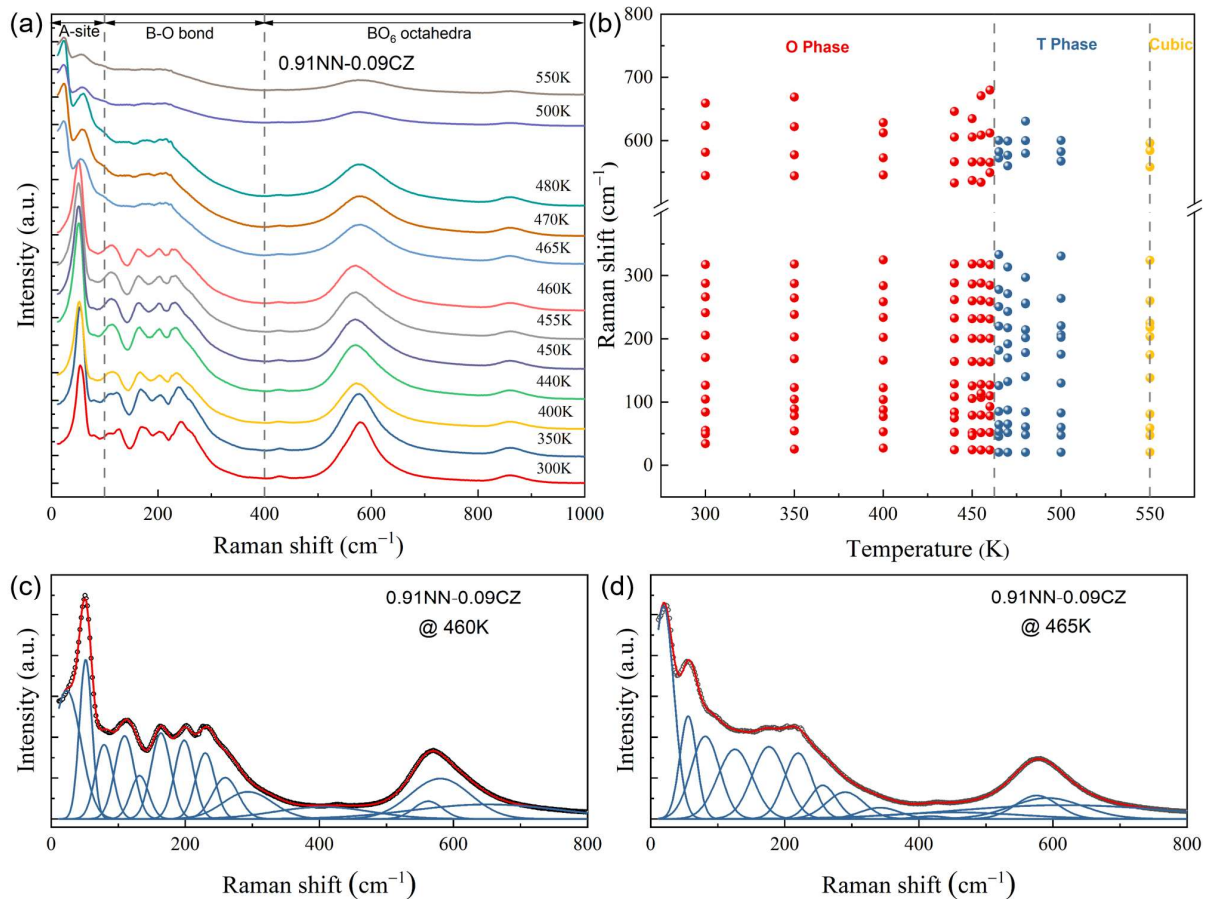

Figure 5. Temperature-dependent (**a**) Raman spectra and (**b**) the wave number of several selected Raman peaks by the multiple peak fitting of Gaussian-Lorentzian functions for 0.91NN-0.09CZ ceramic. Raman Gaussian-Lorentzian fitting of the 0.91NN-0.09CZ sample at (**c**) 460 K and (**d**) 465 K.

4. Conclusions

In summary, this study proposes a novel NTE mechanism caused by the antiferroelectric phase transition of lead-free perovskite materials. By measuring the expansion characteristics of 0.91NN-0.09CZ ceramic and analyzing the temperature-dependent XRD and Raman scattering data, the relationship between the antiferroelectric phase transition and the abnormal NTE behavior of NN-based ceramics is revealed. Dielectric measurements prove that the phase transition temperature decreases with the doping of CZ. The phase transition from the antiferroelectric orthorhombic P phase to the antiferroelectric tetragonal W phase leads to the contraction of the *a*-axis and the enhancement of the tetragonality, resulting in abnormal NTE behavior. The present work shows that NTE can be induced by the antiferroelectric phase transition of lead-free perovskite ceramics, which provides new insights for understanding the mechanism of NTE and is important for the exploration of new compounds with NTE.

Author Contributions: Conceptualization, H.Y. and L.C.; methodology, H.Y.; validation, H.Y.; resources, H.Q.; data curation, H.Y.; writing—original draft preparation, H.Y.; writing—review and editing, L.C., C.Z., and H.Q.; funding acquisition, H.Q. and C.Z. All authors have read and agreed to the published version of the manuscript.

Conflicts of Interest: The authors declare no conflict of interest.

References

1. Bhalla, A.; Guo, R.; Roy, R. The perovskite structure—A review of its role in ceramic science and technology. *Mater. Res. Innov.* **2000**, *4*, 3–26. [CrossRef]
2. Yuzyuk, Y.I. Raman scattering spectra of ceramics, films, and superlattices of ferroelectric perovskites: A review. *Phys. Solid State* **2012**, *54*, 1026–1059. [CrossRef]
3. Jaffe, B.; Roth, R.; Marzullo, S. Piezoelectric properties of lead zirconate-lead titanate solid-solution ceramics. *J. Appl. Phys.* **1954**, *25*, 809–810. [CrossRef]
4. Sawaguchi, E. Ferroelectricity versus antiferroelectricity in the solid solutions of $PbZrO_3$ and $PbTiO_3$. *J. Phys. Soc. Jpn.* **1953**, *8*, 615–629. [CrossRef]
5. Yamamoto, T.Y.T. Ferroelectric properties of the $PbZrO_3$–$PbTiO_3$ system. *Jpn. J. Appl. Phys.* **1996**, *35*, 5104. [CrossRef]
6. Wang, K.; Li, J.-F. (K,Na)NbO_3-based lead-free piezoceramics: Phase transition, sintering and property enhancement. *J. Adv. Ceram.* **2012**, *1*, 24–37. [CrossRef]
7. Wu, J. Perovskite lead-free piezoelectric ceramics. *J. Appl. Phys.* **2020**, *127*, 190901. [CrossRef]
8. Saito, Y.; Takao, H.; Tani, T.; Nonoyama, T.; Takatori, K.; Homma, T.; Nagaya, T.; Nakamura, M. Lead-free piezoceramics. *Nature* **2004**, *432*, 84–87. [CrossRef]
9. Zheng, T.; Wu, J.; Xiao, D.; Zhu, J. Recent development in lead-free perovskite piezoelectric bulk materials. *Prog. Mater. Sci.* **2018**, *98*, 552–624. [CrossRef]
10. Xiao, D. Progresses and further considerations on the research of perovskite lead-free piezoelectric ceramics. *J. Adv. Dielectr.* **2011**, *1*, 33–40. [CrossRef]
11. Park, S.-E.; Shrout, T.R. Ultrahigh strain and piezoelectric behavior in relaxor based ferroelectric single crystals. *J. Appl. Phys.* **1997**, *82*, 1804–1811. [CrossRef]
12. Haertling, G.H. Ferroelectric Ceramics: History and Technology. *J. Am. Ceram. Soc.* **1999**, *82*, 797–818. [CrossRef]
13. Choi, S.W.; Shrout, R.T.; Jang, S.J.; Bhalla, A.S. Dielectric and pyroelectric properties in the Pb ($Mg_{1/3}Nb_{2/3}$)O_3-$PbTiO_3$ system. *Ferroelectrics* **1989**, *100*, 29–38. [CrossRef]
14. Wang, X.; Chao, X.; Liang, P.; Wei, L.; Yang, Z. Polymorphic phase transition and enhanced electrical properties of ($Ba_{0.91}Ca_{0.09-x}Sr_x$)($Ti_{0.92}Sn_{0.08}$)O_3 lead-free ceramics. *Ceram. Int.* **2014**, *40*, 9389–9394. [CrossRef]
15. Ray, G.; Sinha, N.; Bhandari, S.; Kumar, B. Excellent piezo-/pyro-/ferroelectric performance of $Na_{0.47}K_{0.47}Li_{0.06}NbO_3$ lead-free ceramic near polymorphic phase transition. *Scr. Mater.* **2015**, *99*, 77–80. [CrossRef]
16. Chen, J.; Hu, L.; Deng, J.; Xing, X. Negative thermal expansion in functional materials: Controllable thermal expansion by chemical modifications. *Chem. Soc. Rev.* **2015**, *44*, 3522–3567. [CrossRef]
17. Evans, J.S.O. Negative thermal expansion materials. *J. Chem. Soc. Dalton Trans.* **1999**, *19*, 3317–3326. [CrossRef]
18. Forrester, J.S.; Kisi, E.H.; Knight, K.S.; Howard, C.J. Rhombohedral to cubic phase transition in the relaxor ferroelectric PZN. *J. Phys. Condens. Matter* **2006**, *18*, L233–L240. [CrossRef]
19. Chen, J.; Fan, L.; Ren, Y.; Pan, Z.; Deng, J.; Yu, R.; Xing, X. Unusual Transformation from Strong Negative to Positive Thermal Expansion in $PbTiO_3$−$BiFeO_3$ Perovskite. *Phys. Rev. Lett.* **2013**, *110*, 115901. [CrossRef]
20. Malič, B.; Razpotnik, H.; Koruza, J.; Kokalj, S.; Cilenšek, J.; Kosec, M. Linear thermal expansion of lead-free piezoelectric $K_{0.5}Na_{0.5}NbO_3$ ceramics in a wide temperature range. *J. Am. Ceram. Soc.* **2011**, *94*, 2273–2275. [CrossRef]
21. Raevski, I.; Prosandeev, S. A new, lead free, family of perovskites with a diffuse phase transition: $NaNbO_3$-based solid solutions. *J. Phys. Chem. Solids* **2002**, *63*, 1939–1950. [CrossRef]
22. Yuzyuk, Y.I.; Simon, P.; Gagarina, E.; Hennet, L.; Thiaudiere, D.; Torgashev, V.I.; Raevskaya, S.I.; Raevskii, I.P.; Reznitchenko, L.A.; Sauvajol, J.L. Modulated phases in $NaNbO_3$: Raman scattering, synchrotron X-ray diffraction, and dielectric investigations. *J. Phys. Condens. Matter* **2005**, *17*, 4977. [CrossRef]
23. Yang, D.; Gao, J.; Shu, L.; Liu, Y.X.; Yu, J.; Zhang, Y.; Wang, X.; Zhang, B.P.; Li, J.F. Lead-free antiferroelectric niobates $AgNbO_3$ and $NaNbO_3$ for energy storage applications. *J. Mater. Chem. A* **2020**, *8*, 23724–23737. [CrossRef]
24. Zhang, H.; Wei, T.; Zhang, Q.; Ma, W.; Fan, P.; Salamon, D.; Zhang, S.-T.; Nan, B.; Tan, H.; Ye, Z.-G. A review on the development of lead-free ferroelectric energy-storage ceramics and multilayer capacitors. *J. Mater. Chem. C* **2020**, *8*, 16648–16667. [CrossRef]
25. Qi, H.; Wang, G.; Zhang, Y.; Wang, D.; Liu, H.; Deng, S.; Zuo, R.; Chen, J. Tunable phase structure in $NaNbO_3$ ceramics by grain-size effect, electric field and heat treatment. *Acta Mater.* **2023**, *248*, 118778. [CrossRef]

26. Shimizu, H.; Guo, H.; Reyes-Lillo, S.E.; Mizuno, Y.; Rabe, K.M.; Randall, C.A. Lead-free antiferroelectric: xCaZrO$_3$-(1 − x)NaNbO$_3$ system (0 ≤ x ≤ 0.10). *Dalton Trans.* **2015**, *44*, 10763–10772. [CrossRef]

27. Qi, H.; Li, W.; Wang, L.; Chen, L.; Liu, H.; Deng, S.; Chen, J. Large (anti)ferrodistortive NaNbO$_3$-based lead-free relaxors: Polar nanoregions embedded in ordered oxygen octahedral tilt matrix. *Mater. Today* **2022**, *60*, 91–97. [CrossRef]

28. Wu, J.; Liu, H.; Qi, H.; Gao, B.; Chen, L.; Li, W.; Deng, S.; Chen, J. Stabilization of the ferrielectric phase in NaNbO$_3$-based lead-free ceramics for a wide-temperature large electrocaloric effect. *J. Mater. Chem. A* **2022**, *10*, 18070–18077. [CrossRef]

29. Dobal, P.S.; Katiyar, R.S. Studies on ferroelectric perovskites and Bi-layered compounds using micro-Raman spectroscopy. *J. Raman Spectrosc.* **2002**, *33*, 405–423. [CrossRef]

30. Tenne, D.A.; Xi, X. Raman Spectroscopy of Ferroelectric Thin Films and Superlattices. *J. Am. Ceram. Soc.* **2008**, *91*, 1820–1834. [CrossRef]

31. Klein, N.; Hollenstein, E.; Damjanovic, D.; Trodahl, H.J.; Setter, N.; Kuball, M. A study of the phase diagram of (K,Na,Li)NbO$_3$ determined by dielectric and piezoelectric measurements, and Raman spectroscopy. *J. Appl. Phys.* **2007**, *102*, 014112. [CrossRef]

32. Rubio-Marcos, F.; Bañares, M.A.; Romero, J.J.; Fernandez, J.F. Correlation between the piezoelectric properties and the structure of lead-free KNN-modified ceramics, studied by Raman Spectroscopy. *J. Raman Spectrosc.* **2011**, *42*, 639–643. [CrossRef]

33. Yuzyuk, Y.I.; Gagarina, E.; Simon, P.; Reznitchenko, L.A.; Hennet, L.; Thiaudiere, D. Synchrotron X-ray diffraction and Raman scattering investigations of (Li$_x$Na$_{1−x}$)NbO$_3$ solid solutions: Evidence of the rhombohedral phase. *Phys. Rev. B* **2004**, *69*, 144105. [CrossRef]

34. Jauhari, M.; Mishra, S.K.; Poswal, H.K.; Mittal, R.; Chaplot, S.L. Evidence of low-temperature phase transition in BaTiO$_3$-modified NaNbO$_3$: Raman spectroscopy study. *J. Raman Spectrosc.* **2019**, *50*, 1949–1955. [CrossRef]

35. Shakhovoy, R.A.; Raevskaya, S.I.; Shakhovaya, L.A.; Suzdalev, A.D.; Raevski, I.P.; Yuzyuk, Y.I.; Semenchev, A.F.; El Marssi, M. Ferroelectric Q and antiferroelectric P phases' coexistence and local phase transitions in oxygen-deficient NaNbO$_3$ single crystal: Micro-Raman, dielectric and dilatometric studies. *J. Raman Spectrosc.* **2012**, *43*, 1141–1145. [CrossRef]

36. Chao, L.; Hou, Y.; Zheng, M.; Yue, Y.; Zhu, M. Macroscopic ferroelectricity and piezoelectricity in nanostructured NaNbO$_3$ ceramics. *Appl. Phys. Lett.* **2017**, *110*, 122901. [CrossRef]

37. Tan, X.; Ma, C.; Frederick, J.; Beckman, S.; Webber, K.G. The Antiferroelectric ↔ Ferroelectric Phase Transition in Lead-Containing and Lead-Free Perovskite Ceramics. *J. Am. Ceram. Soc.* **2011**, *94*, 4091–4107. [CrossRef]

38. Mishra, S.K.; Mittal, R.; Pomjakushin, V.Y.; Chaplot, S.L. Phase stability and structural temperature dependence in sodium niobate: A high-resolution powder neutron diffraction study. *Phys. Rev. B* **2011**, *83*, 134105. [CrossRef]